Research Article | Vol. 9, No. 3 | 1 Mar 2018 | BIOMEDICAL OPTICS EXPRESS 1309
Biomedical Optics EXPRESS

Spectroscopic photoacoustic imaging of radiofrequency ablation in the left atrium

SOPHINESE ISKANDER-RIZK,[1,*] PIETER KRUIZINGA,[1,2] ANTONIUS F. W. VAN DER STEEN,[1,2] AND GIJS VAN SOEST[1]

[1]*Biomedical Engineering Department, Thorax Center-Erasmus MC, Wytemaweg 80, 3015 CN Rotterdam, The Netherlands*
[2]*ImPhys, Faculty of Applied Sciences, Delft University of Technology, Lorentzweg 1, 2628 CJ Delft, The Netherlands*
**s.iskander-rizk@erasmusmc.nl*

Abstract: Catheter-based radiofrequency ablation for atrial fibrillation has long-term success in 60-70% of cases. A better assessment of lesion quality, depth, and continuity could improve the procedure's outcome. We investigate here photoacoustic contrast between ablated and healthy atrial-wall tissue in vitro in wavelengths spanning from 410 nm to 1000 nm. We studied single- and multi-wavelength imaging of ablation lesions and we demonstrate that a two-wavelength technique yields precise detection of lesions, achieving a diagnostic accuracy of 97%. We compare this with a best single-wavelength (640 nm) analysis that correctly identifies 82% of lesions. We discuss the origin of relevant spectroscopic features and perspectives for translation to clinical imaging.

OCIS codes: (170.5120) Photoacoustic imaging; (170.6935) Tissue characterization; (170.6510) Spectroscopy, tissue diagnostics; (100.2980) Image enhancement;.

References and links

1. J. Heeringa, D. A. M. van der Kuip, A. Hofman, J. A. Kors, G. van Herpen, B. H. C. Stricker, T. Stijnen, G. Y. H. Lip, and J. C. M. Witteman, "Prevalence, incidence and lifetime risk of atrial fibrillation: the Rotterdam study," Eur. Heart J. **27**(8), 949–953 (2006).
2. A. Bajpai, I. Savelieva, and A. J. Camm, "Epidemiology and economic burden of atrial fibrillation," US Cardiovasc Dis **1**, 14–17 (2007).
3. S. H. Hohnloser and Y. G. Li, "Drug treatment of atrial fibrillation: What have we learned?" Curr. Opin. Cardiol. **12**(1), 24–32 (1997).
4. C. Blomström-Lundqvist, M. M. Scheinman, E. M. Aliot, J. S. Alpert, H. Calkins, A. J. Camm, W. B. Campbell, D. E. Haines, K. H. Kuck, B. B. Lerman, D. D. Miller, C. W. Shaeffer, Jr., W. G. Stevenson, G. F. Tomaselli, E. M. Antman, S. C. Smith, Jr., J. S. Alpert, D. P. Faxon, V. Fuster, R. J. Gibbons, G. Gregoratos, L. F. Hiratzka, S. A. Hunt, A. K. Jacobs, R. O. Russell, Jr., S. G. Priori, J. J. Blanc, A. Budaj, E. F. Burgos, M. Cowie, J. W. Deckers, M. A. A. Garcia, W. W. Klein, J. Lekakis, B. Lindahl, G. Mazzotta, J. C. A. Morais, A. Oto, O. Smiseth, and H. J. Trappe; American College of Cardiology; American Heart Association Task Force on Practice Guidelines; European Society of Cardiology Committee for Practice Guidelines. Writing Committee to Develop Guidelines for the Management of Patients With Supraventricular Arrhythmias, "ACC/AHA/ESC guidelines for the management of patients with supraventricular arrhythmias - Executive summary a report of the American College of Cardiology/American Heart Association Task Force on Practice Guidelines and the European Society of Cardiology Committee for Practice Guidelines (writing committee to develop guidelines for the management of patients with supraventricular arrhythmias)," Circulation **108**(15), 1871–1909 (2003).
5. L. Ganjehei, M. Razavi, and A. Rasekh, "Catheter-based ablation of atrial fibrillation: a brief overview," Tex. Heart Inst. J. **38**(4), 361–363 (2011).
6. M. Wright, "Real-time atrial wall imaging," Heart Rhythm **12**(8), 1836–1837 (2015).
7. A. C. Lardo, E. R. McVeigh, P. Jumrussirikul, R. D. Berger, H. Calkins, J. Lima, and H. R. Halperin, "Visualization and temporal/spatial characterization of cardiac radiofrequency ablation lesions using magnetic resonance imaging," Circulation **102**(6), 698–705 (2000).
8. R. J. Hunter, D. A. Jones, R. Boubertakh, L. C. Malcolme-Lawes, P. Kanagaratnam, C. F. Juli, D. W. Davies, N. S. Peters, V. Baker, M. J. Earley, S. Sporton, L. C. Davies, M. Westwood, S. E. Petersen, and R. J. Schilling, "Diagnostic Accuracy of Cardiac Magnetic Resonance Imaging in the Detection and Characterization of Left Atrial Catheter Ablation Lesions: A Multicenter Experience," J. Cardiovasc. Electrophysiol. **24**(4), 396–403 (2013).

#309967 https://doi.org/10.1364/BOE.9.001309
Journal © 2018 Received 26 Oct 2017; revised 16 Jan 2018; accepted 31 Jan 2018; published 23 Feb 2018

Biomedical Optics EXPRESS

9. C. P. Fleming, L. M. Barwick, K. J. Quan, and A. M. Rollins, "In-Vitro Characterization of Ablation Lesions Using Oct," Circulation **118**, S831–S832 (2008).
10. R. P. Singh-Moon, C. C. Marboe, and C. P. Hendon, "Near-infrared spectroscopy integrated catheter for characterization of myocardial tissues: preliminary demonstrations to radiofrequency ablation therapy for atrial fibrillation," Biomed. Opt. Express **6**(7), 2494–2511 (2015).
11. D. A. Gil, L. M. Swift, H. Asfour, N. Muselimyan, M. A. Mercader, and N. A. Sarvazyan, "Autofluorescence hyperspectral imaging of radiofrequency ablation lesions in porcine cardiac tissue," J. Biophotonics **10**(8), 1008–1017 (2016).
12. M. Granier, P. F. Winum, M. Granier, P. Liaud, G. Cayla, P. Messner, J.-L. Pasquie, and I. Schuster, "Real-time atrial wall imaging during radiofrequency ablation in a porcine model," Heart Rhythm **12**(8), 1827–1835 (2015).
13. T. Szili-Torok, G. P. Kimman, D. Theuns, J. Res, J. R. Roelandt, and L. J. Jordaens, "Visualisation of intra-cardiac structures and radiofrequency lesions using intracardiac echocardiography," Eur. J. Echocardiogr. **4**(1), 17–22 (2003).
14. M. Wright, E. Harks, S. Deladi, F. Suijver, M. Barley, A. van Dusschoten, S. Fokkenrood, F. Zuo, F. Sacher, M. Hocini, M. Haïssaguerre, and P. Jaïs, "Real-time lesion assessment using a novel combined ultrasound and radiofrequency ablation catheter," Heart Rhythm **8**(2), 304–312 (2011).
15. J. F. Ren, F. E. Marchlinski, D. J. Callans, and E. S. Zado, "Echocardiographic lesion characteristics associated with successful ablation of inappropriate sinus tachycardia," J. Cardiovasc. Electrophysiol. **12**(7), 814–818 (2001).
16. S. A. Eyerly, M. Vejdani-Jahromi, D. M. Dumont, G. E. Trahey, and P. D. Wolf, "The Evolution of Tissue Stiffness at Radiofrequency Ablation Sites During Lesion Formation and in the Peri-Ablation Period," J. Cardiovasc. Electrophysiol. **26**(9), 1009–1018 (2015).
17. W. Shi, A. Anand, S. Sethuraman, S. W. Huang, H. Xie, H. Agarwal, P. Yan, J. Azevedo, J. Kruecker, G. Ng, V. Shamdasani, W. Pritchard, J. Karanian, and B. Wood, "Monitoring of Radiofrequency Ablation with Shear Wave Delay Mapping," in Proceedings of IEEE International Ultrasonics Symposium (IEEE,2015).
18. W. Kwiecinski, J. Provost, R. Dubois, F. Sacher, M. Haïssaguerre, M. Legros, A. Nguyen-Dinh, R. Dufait, M. Tanter, and M. Pernot, "Quantitative evaluation of atrial radio frequency ablation using intracardiac shear-wave elastography," Med. Phys. **41**(11), 112901 (2014).
19. G. A. Pang, E. Bay, X. L. Deán-Ben, and D. Razansky, "Three-Dimensional Optoacoustic Monitoring of Lesion Formation in Real Time During Radiofrequency Catheter Ablation," J. Cardiovasc. Electrophysiol. **26**(3), 339–345 (2015).
20. N. Dana, L. Di Biase, A. Natale, S. Emelianov, and R. Bouchard, "In vitro photoacoustic visualization of myocardial ablation lesions," Heart Rhythm **11**(1), 150–157 (2014).
21. G. M. Hale and M. R. Querry, "Optical constants of water in the 200-nm to 200-μm wavelength region," Appl. Opt. **12**(3), 555–563 (1973).
22. J. S. Prahl Scott, "Optical absorption of water compendium" (2017), retrieved 17–07–2017, 2017, http://omlc.org/spectra/water/abs/index.html.
23. S. K. S. Huang and M. A. Wood, *Catheter Ablation of Cardiac Arrhythmias* E-book (Elsevier Health Sciences, 2014).
24. J. Swartling, S. Pålsson, P. Platonov, S. B. Olsson, and S. Andersson-Engels, "Changes in tissue optical properties due to radio-frequency ablation of myocardium," Med. Biol. Eng. Comput. **41**(4), 403–409 (2003).
25. P. Tomicki, Thermal stability and color change of myoglobin in model systems (University of Guelph, 1999).
26. M. C. Hunt, O. Sørheim, and E. Slinde, "Color and heat denaturation of myoglobin forms in ground beef," J. Food Sci. **64**(5), 847–851 (1999).
27. L. Kristensen and H. J. Andersen, "Effect of heat denaturation on the pro-oxidative activity of metmyoglobin in linoleic acid emulsions," J. Agric. Food Chem. **45**(1), 7–13 (1997).
28. R. H. Bremmer, A. Nadort, T. G. van Leeuwen, M. J. C. van Gemert, and M. C. G. Aalders, "Age estimation of blood stains by hemoglobin derivative determination using reflectance spectroscopy," Forensic Sci. Int. **206**(1-3), 166–171 (2011).
29. B. Burstein and S. Nattel, "Atrial fibrosis: Mechanisms and clinical relevance in atrial fibrillation," J. Am. Coll. Cardiol. **51**(8), 802–809 (2008).
30. F. Bettelheim, W. Brown, M. Campbell, S. Farrell, and O. Torres, *Introduction to General, Organic and Biochemistry* (Nelson Education, 2012).
31. S. K. V. Sekar, I. Bargigia, A. D. Mora, P. Taroni, A. Ruggeri, A. Tosi, A. Pifferi, and A. Farina, "Diffuse optical characterization of collagen absorption from 500 to 1700 nm," J. Biomed. Opt. **22**(1), 015006 (2017).
32. J. J. Xia, A. Weaver, D. E. Gerrard, and G. Yao, "Heating induced optical property changes in beef muscle," J. Food Eng. **84**(1), 75–81 (2008).
33. H. Aupperle, N. Doll, T. Walther, C. Ullmann, H. A. Schoon, and F. Wilhelm Mohr, "Histological findings induced by different energy sources in experimental atrial ablation in sheep," Interact. Cardiovasc. Thorac. Surg. **4**(5), 450–455 (2005).

Biomedical Optics EXPRESS

1. Introduction

1.1 Atrial fibrillation

Atrial fibrillation (AF) is a cardiac arrhythmia which arises as a result of electrical activation patterns originating from the atrial wall, rather than the sino-atrial node. The atrium contracts more frequently and asynchronous from the ventricles, leading to reduced overall pump efficiency and vortex flow. Approximately 5% of people over 55 in western countries suffer from AF, while prevalence increases with age [1, 2]. The pathology is associated with a variety of cardiovascular symptoms, such as a higher probability of thromboembolism and stroke, and heart failure, unfolding into increased mortality. Current treatment strategies include pharmaceutical treatment, surgical interventions, and minimally-invasive catheter-based ablation.

In catheter-based radiofrequency (RF) ablation, errant conduction loops are interrupted by inducing tissue necrosis through application of thermal energy. The scar tissue that subsequently forms is non-conductive and effects restoration of a regular contraction pattern. Patients who do not respond to pharmaceutical therapy (~60% [3],), or who are at high risk for surgery, are candidates for catheter-based ablation. It is also advised as a more economical alternative for therapy in younger patients, who would otherwise require lifelong medication [4]. However, current catheter-based ablation procedures have a success rate of about 60-70% [5]. The intervention frequently fails as a result of tissue electrical reconduction, arising in the days, weeks or months after ablation. Causes for reconduction are insufficient ablation, ablation gaps and tissue remodeling. On the other hand, complications due to over-ablation include venous stenosis, thrombus formation, and tamponade; which explains the tendency for interventionists to err on the side of caution and ablate conservatively. Feedback on lesion progression is currently indirect: lesion extent is assessed via impedance changes, as well as temperature and contact force values, all measured at the catheter tip. Finally, the end point of ablation is determined by the cessation of electrical activity at the ectopic foci after pacing. Better monitoring and control of the ablation process, quantifying both extent and functionality of the lesion is one way to reduce the duration and improve the outcome of the procedure [6].

1.2 RF ablation lesion imaging in the literature

In the quest of improving the success rate of catheter-based ablation procedures, much research has been directed towards assessment of the lesions created by ablation. Multiple imaging modalities have been explored; the most successful thus far being CMR (cardiac magnetic resonance) gadolinium enhanced imaging. However, CMR, compared to other imaging modalities, is difficult to apply during an intervention, as it requires an MRI-equipped cardiac electrophysiology catheterization room, and MRI-compatible instruments [7]. It has mediocre image resolution (resolution cell ≈1-2 mm ≈atrial wall depth), leading to a poor assessment of lesion area, volume and transmurality [8], and is relatively expensive.

Optical methods which were explored for lesion imaging include Optical Coherence Tomography (OCT) [9], Near Infrared Spectroscopy (NIRS) [10] and auto-Fluorescence Hyperspectral Imaging (aHSI) [11]. These methods are based on scattered, reflected and emitted light from the tissue. However, despite demonstration of contrast between lesion and non-ablated tissue in all three modalities, they lack reliable evaluation of lesion extent in depth.

Other imaging modalities that were explored for ablation lesion monitoring are conventional ultrasound [12–15] as well as ultrasound elastography [16–18]. Visibility of lesions on grayscale ultrasound has been disputed in literature, with contradictory reports of both decrease and increase in echogenicity in lesion areas. Elastography, on the other hand, seems more successful at lesion identification and looks quite promising. However, monitoring lesion progression with shear wave elastography is still a challenge due to the

Biomedical Optics EXPRESS

estimation of atrial wall curvature for wave propagation progression and the difficulty in aligning the ultrasound beam to the lesion site across the ablation catheter [18].

1.3 Photoacoustic imaging for lesion progression monitoring

Previous studies have shown optical, mechanical as well as acoustic contrast between lesions and the remaining non-ablated tissue; yet the challenge of the development of an accurate lesion delineation method that is easily translatable to the clinical setting remains. Photoacoustic (PA) imaging incorporates all aforementioned types of contrast. The PA source pressure $p_0(z) = \Gamma(z)\cdot\mu_a(z,\lambda)\cdot F(z,\lambda)$ is the product of the local optical fluence F, the local optical absorption coefficient μ_a, and the Grüneisen coefficient Γ. The absorption and fluence depend on wavelength and tissue optical properties. The Grüneisen coefficient is the conversion factor between optical energy to thermo-elastic strain, and potentially provides information on tissue stiffness and temperature. PA imaging is unique in its access to such a wide array of tissue properties, which may play a role in lesion characterization.

Intracardiac echo (ICE) is frequently used to guide septal puncture in ablation procedures for atrial fibrillation. The ultrasound catheter, with a typical center frequency of about 7 MHz, could also be used for detection of PA signals if light could be delivered through a modified ablation catheter for instance. The potential for clinical translation and enhanced contrast encouraged us to look further into photoacoustic imaging as a means of monitoring lesion formation.

Two groups have previously performed PA imaging of RF ablation lesions on porcine cardiac tissue ex-vivo [19, 20]. Pang et al. [19] have identified a maximum lesion to non-ablated tissue contrast at 780 nm using a 3 MHz transducer. Dana et al. [20] revealed a spectral signature providing contrast at wavelengths near 760 nm (which was attributed to the hemoglobin spectral signature disappearing) using a 21 MHz transducer. Both studies evaluated lesion formation in ventricular tissue, which is not directly generalizable to atrial ablation.

In this study we analyze the PA signal from healthy and ablated porcine left atrial tissue including endocardial and epicardial layers. We acquired PA signals with a linear array transducer of center frequency matching that of ICE catheters to verify bandwidth compatibility. We performed PA spectroscopic imaging prior to, and after ablation. We identify the spectral changes between fresh and ablated tissue in order to visualize the induced changes in tissue composition, as well as identify wavelengths for optimal contrast, imaging depth and signal to noise ratio (SNR). We demonstrate robust contrast for identification of ablation lesions and quantify the diagnostic accuracy by computing the receiver-operator curve for lesion detection, using either a single wavelength or an optimal combination of two wavelengths.

2. Materials and methods

2.1 Sample materials and tissue handling

We evaluated PA image contrast after RF ablation of fresh excised porcine left atria (0-24 h post mortem), obtained from a local butcher and from the Dept. of Experimental Cardiology in our institute. We collected 23 spectra (23 lesions) from 14 different tissue samples originating from 12 different hearts. The average thickness of the examined tissues was 2.7 mm with a maximum of 8 mm and a minimum of 400 μm, as measured from ultrasound images.

Tissues were mounted in a water tank, suspended by wires. For ablation we used an EPT 1000 XP APM system (Boston Scientific, Marlborough, Massachusetts, United States) with a Blazer II HTD, Asym #4 (model: 5031 THN4) catheter. We delivered ablation energy to localized site(s) of the endocardium in the imaging plane, using appropriate settings (Power ≥ 20W, Temperature ≥ 60°C, time ≥ 20s). We kept ablating the same lesion site (n ≥ 1) until a

Biomedical Optics EXPRESS

visible lesion was produced on the endocardium side. After PA imaging, we sectioned the tissue through the lesion for visual inspection. We determined the imaged plane by inserting needles that are visible on the ultrasound image. Throughout the measurement, the tissue was kept in a HEPES buffer mixed with saline solution of pH 7.4 at room temperature.

2.2 Setup description

We performed photoacoustic spectroscopy with a pulsed laser source tuned from 410 nm to 708 nm, and 712 nm to 1000 nm (Vibrant B-355II, Opotek, Santa Clara, CA, USA) in steps of 2 nm. The setup consisted of a linear array transducer (192 channels, L12-3v, f_c = 7.8 MHz, Verasonics, Kirkland, Washington) connected to a Verasonics Vantage 256 research system. The acquisition was programmed to overlay images created from pulse echo plane wave ultrasound (US) at 3 different angles (–18°,0, + 18°), and from photoacoustic signals averaged over 6 laser pulses. During the photoacoustic acquisition, the time-gain compensation (TGC) was set to its maximum value (not changing with depth), to optimize examination of the signal attenuation with depth. The tissue was mounted in a transmission-mode PA setup [Fig. 1], with the endocardium facing a broad illumination source. We performed spectroscopic imaging, before and after ablating the tissue, keeping the relative position of the tissue and the transducer as stable as possible, in order to compare the signal before and after ablation from the same portion of tissue. After acquiring tissue spectroscopy data, we measured the OPO tuning curve for calibration of the PA signal. The fluence varied between 0.3 and 1 mJ/cm^2 depending on the wavelength.

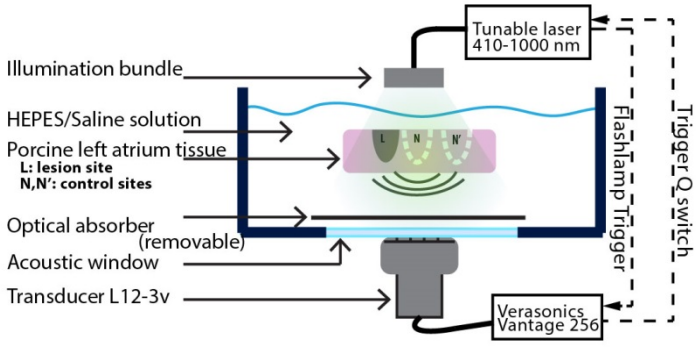

Fig. 1. Transmission PA imaging setup for spectroscopic analysis of RF ablation lesions. The tissue is suspended and stretched with the aid of wires. A fiber bundle illuminates the atrium sample from the endocardial side. A 192 element 7.8 MHz center frequency transducer records the generated PA signal. A black plastic sheet (optical absorber) provides a reference signal to assess optical attenuation. We analyze spectroscopic differences in PA response in lesion (L) and control (N,N') sites.

2.3 Extraction and validation of photoacoustic spectra

From the beamformed photoacoustic images, we averaged the intensity (I) in a user-defined image region of interest (ROI, I_{ROI}), as a function of excitation wavelength. We identified regions in co-registered images generated prior to and after ablation. The lesion position was identified as the location of the ablation catheter and the lesion extent was defined from the visual inspection of the tissue cross section after the experiment. In post-ablation images, we selected two regions, a lesion site (L, post) and a non-ablated site (N/N', post). Definition of ROIs on the illuminated endocardial side minimizes the impact of spectral coloring when evaluating the tissue spectral photoacoustic features. ROI size ranged from 3 × 3 pixels (= 0.3 × 0.6 mm axial × lateral) to 10 × 10 pixels (= 1 × 2 mm) depending on visual lesion size.

We averaged all spectra extracted from three identified region classes: lesion (L, post), lesion site prior to ablation (L, pre), and control after ablation (N, post), shown in Fig. 2. We

Biomedical Optics EXPRESS

equalized the means across the spectrum to account for day-to-day variations prior to averaging all the traces and computing the standard deviations. We also normalized to the OPO tuning curve verified after each experiment. We validated our methodology by corroborating the water absorption spectrum at the water-air interface to those reported in the literature [21, 22].

We assessed spectral optical attenuation by recording the signal form a highly absorbing black plastic phantom behind the tissue as shown in Fig. 1. Reliable volumetric imaging of ablation lesions is only possible in those spectral regions that allow sufficient penetration of excitation light. Wavelengths which reliably generate a signal from the black target behind the tissue are suitable for transmural imaging, which was true for $\lambda > 600$ nm, reflecting the familiar decrease of optical attenuation with increasing wavelength.

2.4 Quantitative evaluation of imaging parameters

2.4.1 Contrast in single wavelength images

We calculated the signal ratio (SR_L) as the ratio I_L/I_N (subscripts refer to the regions as indicated in Fig. 1) on post-ablation images, which characterizes lesion contrast with neighboring tissue. We observed that at most wavelengths in our investigated spectral range, the PA signal increased by ablation (independent of temperature), in agreement with literature, so normally $SR_L > 1$. In our data set, we have included multiple different tissue and lesion models (i.e. superficial lesions, tissue slabs with 1 to 3 lesions, trabeculae structure). The mean of the collected SR from all lesion samples thus reflects the general signal contrast due to the ablation process, and the standard deviation indicates the expected variability in this contrast due to different tissue types and ablation strategies. The SR_N for non-lesion sites is a control variable to estimate the variability in signal within one tissue sample among different non-ablated sites. The SR_N was computed as the signal ratio between two different control areas $I_N/I_{N'}$ on post-ablation images; the mean provides information about the signal variation across the tissue due to the tissue intra variability and the standard deviation is caused by the variation in signal due to different left atrium tissue sites.

2.4.2 Wavelength selection criteria for dual wavelength imaging

We explored a dual wavelength imaging method, which takes the ratio of two subsequent frames acquired at different wavelengths, aiming at differentiating lesion sites from untreated tissue. The final dual wavelength image was obtained by subtracting the mean noise value from the overall image to equalize the background among the data set acquired. The rationale behind a two color imaging method is to develop an easily interpretable image that directly identifies and delineates ablation lesions. A two-color ratio image would be insensitive to both temperature effects, and, if the two wavelengths are sufficiently closely spaced, to variation in fluence due to tissue attenuation, approximating $p_0(z,\lambda_1) / p_0(z,\lambda_2) = \mu_a(z,\lambda_1) / \mu_a(z,\lambda_2)$. A dual wavelength imaging method would eliminate the need for modeling the impact of tissue optics or temperature (which both change during ablation) on the photoacoustic signal.

In order to determine the wavelength pair that provides the highest, most reliable lesion contrast, we first defined the two-wavelength signal ratio for control ($\varnothing_N$) and lesion ($\varnothing_L$) areas:

$$\varnothing_N = \frac{I_N(\lambda_1)}{I_N(\lambda_2)} \tag{1}$$

$$\varnothing_L = \frac{I_L(\lambda_1)}{I_L(\lambda_2)}, \tag{2}$$

Biomedical Optics EXPRESS

We restricted the wavelengths to 630 nm < λ < 1000 nm to ensure a homogeneous illumination in a slab of 3 mm by excluding highly attenuated wavelengths, and avoiding the spectral range around the OPO tuning gap, near 709 nm (702-724 nm, because of low output fluence < 0.3 mJ/cm^2 and thus limited SNR). Variability in medium optical properties can be prevented by limiting the spectral separation between the two wavelengths.

We then determined the best pair of wavelengths for a ratio image by evaluating:

$$\{\lambda_1, \lambda_2\} = \arg \max_{\Delta\lambda<150\text{nm}} \frac{\varnothing_L}{\varnothing_N}, \text{such that} \frac{\varnothing_L}{\varnothing_N} > 2 \cdot \sigma\left(\frac{\varnothing_L}{\varnothing_N}\right) \tag{3}$$

$\langle\cdot\rangle$ denotes the mean over all measurements. Images constructed from the PA signal at an optimal combination of two wavelengths highlight lesions against a background of unaffected tissue. Equation (3) maximizes the contrast between these two tissue classes, while limiting the variability due to the disparity of tissue and ablation strategy.

2.4.3 Evaluation of dual and single wavelength images for lesion contrast

We evaluated contrast between lesion areas and neighboring tissue after ablation in single and dual wavelength imaging by receiver-operator characteristic (ROC) analysis. Such analysis estimates the visibility of lesions in stand-alone images acquired at the end of ablation or at the beginning of a redo procedure. We calculated the number of true positives (TP; correctly identified lesions) in a dual wavelength image, as the amount of lesion sets for which the ratio exceeds a certain threshold $\varnothing_{\text{thr}}$:

$$\varnothing_{L,\text{post}} > \varnothing_{\text{thr}}. \tag{4}$$

We also calculated the number of false positives (FP) as the amount of control areas satisfying the threshold criterion:

$$\varnothing_{N,\text{post}} > \varnothing_{\text{thr}}. \tag{5}$$

In single-wavelength images, the TP are defined as lesions sites which SR_L (see Sect. 2.4.1) exceeds the threshold ratio Z_{thr}, while false positives are control areas SR_N meeting that norm. We divided the number of TP and FP observations by the number of lesion samples we have collected to obtain TP/FP rates. The total number of controls was equal to the number of lesions collected.

The imaged quantities are different for both imaging approaches: in a dual wavelength approach the pixel represents *a ratio* of PA amplitudes while in single wavelengths a pixel represents an absolute PA signal amplitude. The diagnostic values sought for both dual and single wavelength images were thus unified to represent the same quantity: a ratio of PA signal amplitude. In dual wavelength imaging, normalization to the frame acquired at 930 nm is inherent to the proposed method; in single wavelength lesion contrast we normalized control and lesion sites to the same control region, (SR_L, SR_N). We reduced the influence of the signal absolute value variability due to experimentation on the ROC analysis by normalization.

2.4.4 Evaluation of dual and single wavelength images for lesion formation

We compared the performance of a dual wavelength to a single wavelength imaging method for detecting whether a lesion has been created. The lesion formation criterion is an evaluation of how visible a lesion is in a frame for a reader who can compare that frame with an image acquired earlier during the ablation procedure. This situation would happen for instance during a real-time monitoring of the lesion forming. Therefore the analysis for lesion formation should involve some sort of comparison between pre and post ablation signals. We

Biomedical Optics EXPRESS

evaluated diagnostic accuracy by ROC analysis. We calculated the number of TP in a dual wavelength image, as in (4) and we defined FP as areas in which this threshold is reached prior to ablation:

$$\varnothing_{L,\mathrm{pre}} > \varnothing_{\mathrm{thr}} \tag{6}$$

In single wavelength images, we can only compare PA signal amplitude in lesion areas post and pre-ablation. We defined the true positives as:

$$Z_L = \frac{I_{L,\mathrm{post}}}{I_{L,\mathrm{pre}}} > Z_{\mathrm{thr}} \tag{7}$$

and the false positives as control areas exceeding this threshold:

$$Z_N = \frac{I_{N,\mathrm{post}}}{I_{N,\mathrm{pre}}} > Z_{\mathrm{thr}} \tag{8}$$

Both Z and $\varnothing$ are amplitude ratios and so are comparable variables. Ideally, the two wavelengths chosen for the dual wavelength images should yield a featureless image prior to ablation, and clearly discernable areas corresponding to lesion sites in post-ablation images. An equivalent representation in a single wavelength imaging scheme would occur if we divide the post-ablation frame with the pre-ablation one.

3. Results

3.1 Photoacoustic signal variation with illumination wavelength

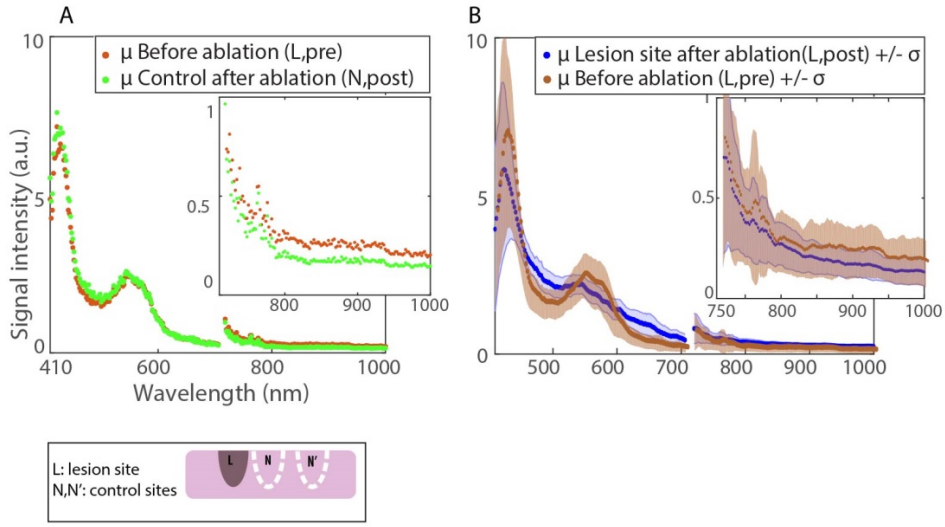

Fig. 2. Average (μ) of spectra extracted from 23 tissue sites. A. Comparison of non-lesion sites before and after ablation. B. Lesion sites before and after ablation.

In Fig. 2, we plot the average of PA signals normalized to the mean variation over the imaging wavelengths at different tissue sites. The orange and green curves in Fig. 2(A) present spectra of non-ablated sites on tissue before and after ablation respectively. These curves show that ablation modifies the spectral absorption features at the ablated site only: the control site after ablation has the same appearance as the lesion before. In the spectra we identify spectral features representing the characteristics of myoglobin with distinctive peaks

Biomedical Optics EXPRESS

at 555 nm and 760 nm. The flattened peak around 550 nm indicates that the observed spectrum is resulting from a mix of oxymyoglobin and myoglobin.

In our spectroscopic characterization of ablation lesions [Figs. 2(A),2(B)] we observe that there are no distinct absorption peaks in the spectral range we investigated, with the exception of that at 420 nm, which appears the same as in the non-ablated tissue. The PA response at wavelengths around 500 and 600 nm is higher than that of fresh tissue. In the near infrared range, as in [20], we find that the lesion is characterized by an attenuation of the 760 nm peak associated with the optical absorption of hemoglobin and myoglobin.

3.2 Imaging parameters

3.2.1 SR and SNR

The most characteristic parameter available for identification and delineation of lesions within a single-wavelength PA image is the SR_L. In Fig. 3, the mean SR_L exceeds the control (SR_N in red) for the range of 600 nm onward. The variability of the SR_L in our data set is large, likely resulting from intrinsic variability in tissue response at different locations. This impacts the reliability of lesion contrast. Nevertheless, from Fig. 3 we can identify the wavelengths for maximum lesion to non-lesion contrast in single wavelength images to be 640, 680, 800 and 730 nm in decreasing contrast. From the transmission measurements using the black absorbing target behind the tissue, we conclude that the imaging range for full tissue illumination ranges from 600 to 1000 nm.

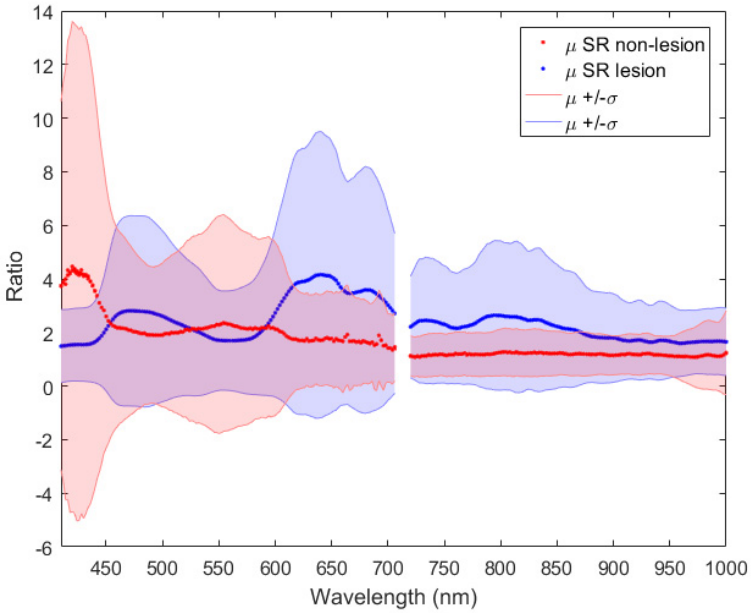

Fig. 3. Variation of the SR across wavelengths for lesion and control sites.

3.3 Imaging lesions

3.3.1 Single wavelength imaging

The analysis in section 3.2 suggests that the most suitable single wavelength for RF ablation lesion imaging, detection and delineation, is 640 nm. Figures 4(A) and 5(A) show PA images of two different tissue samples (Figs. 4(D), 5(D)), pre- and post-ablation at selected wavelengths including 640 nm. In Fig. 4, two lesions were made, while in Fig. 5, a single lesion is present. The photoacoustic images are normalized to the 95th percentile and

Biomedical Optics EXPRESS

displayed on a logarithmic scale. Inspection of the single-wavelength images in Figs. 4(A/C1) and 5(A/C1) shows that there is a variable increase of PA contrast in lesion sites by 2—10 dB, as observed in the SR assessment. In Fig. 4(A), focal enhancements can be appreciated in ablated sites, while in Fig. 5(A), there appears to be a homogeneous signal increase after ablation.

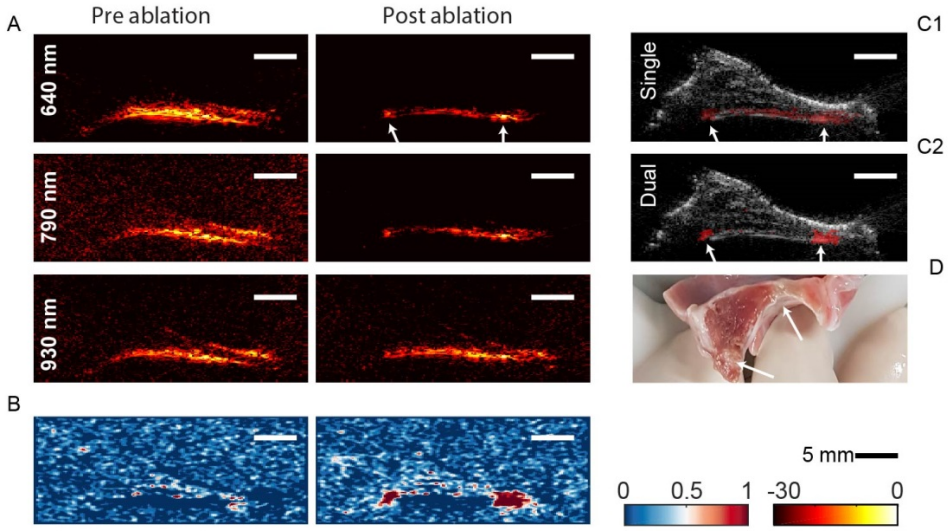

Fig. 4. A. Pre- and post-ablation PA images of a tissue sample at 640, 790 and 930 nm. B. Dual wavelength images pre- and post-ablation. C. Single wavelength (C1, Visualization 1) and dual wavelength (C2) images overlaid on ultrasound. D. Photo of the tissue sample. Arrows point at the ablation sites

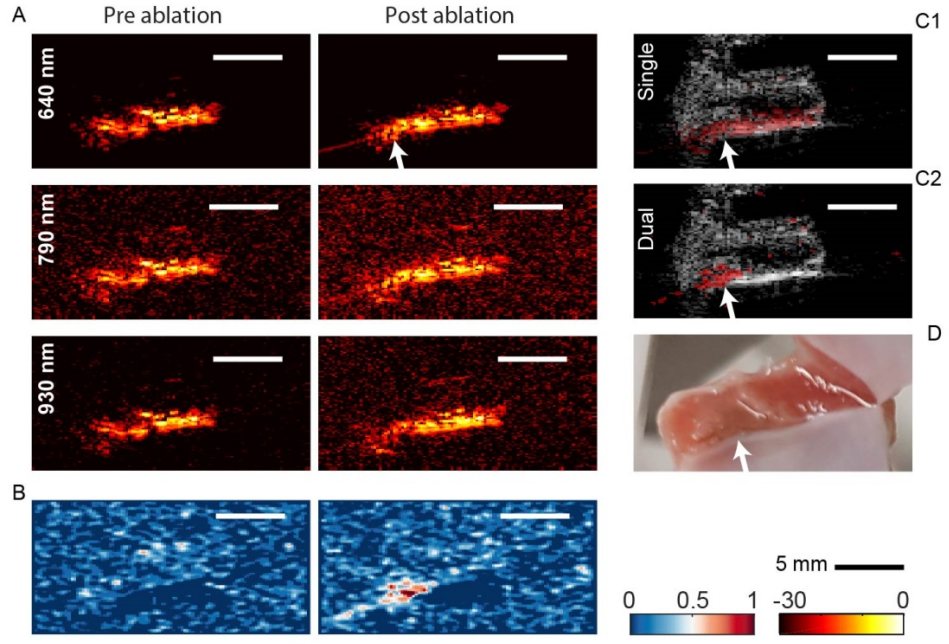

Fig. 5. A. Pre- and post-ablation PA images of a tissue sample at 640, 790 and 930 nm. B. Dual wavelength images pre- and post-ablation. C. Single wavelength (C1) and dual wavelength (C2) images overlaid on ultrasound. D. Photo of the tissue sample. The arrow points at the ablation site.

Biomedical Optics EXPRESS

A movie of the ablation process in the right-hand lesion site in Fig. 4 is available as Visualization 1 [Fig. 4(C1)] . The frame rate is ~0.4/s. We observe a slight increase in tissue thickness during ablation on ultrasound imaging. In the video, the lesion progress is perceptible as a gradual increase in PA signal but the lesion extent is poorly visible. Single wavelengths PA images acquired after the tissue cooled down show that the signal increase observed in Visualization 1 is not necessarily permanent. In Fig. 5(A), the lesion is indiscernible from the surrounding tissue. Lesion visibility was inconsistent over the data sets we have collected, reflecting the high standard deviations observed in our analysis in 3.2.

3.3.2 Dual wavelength imaging

The slope of the signal variation with wavelengths in the near infrared range is different in the lesion areas than that in the non-ablated areas (Fig. 2). We investigate the utility of this difference for identification of lesions by taking the ratio of signals at two wavelengths to distinguish lesion from untreated tissue. We evaluate the ratio of two-wavelength contrast ratios $\varnothing_L / \varnothing_N$ as described in 2.4.2, which we display in Fig. 6. We look for maxima in this matrix, excluding the range where the standard deviation is greater than half the mean (white border), which would lead to increased sensitivity to the innate variability identified previously. The optimal wavelength pair emerging from this analysis is 790 +/- 10 nm and 930 +/- 10 nm.

We evaluate the imaging performance of a dual wavelength ratio imaging method using this optimal pair. We divide the fluence-corrected PA image at 790 nm by that acquired at 930 nm in both pre- and post-ablation acquisitions. We create images from this ratio, subtracting the background, which arises from the (variable) noise in the PA image. Images of the example tissues we examined before are shown in Figs. 4(B) and 5(B). We observe that on pre-ablation images we see a uniform signal indicating the absence of lesions, and on post-ablation images we see bright signal at the lesion spots. In Fig. 5, the lesion was not visible on any of the single wavelength post-ablation images, but becomes quite clear with the dual wavelength ratio imaging method. Figure 4(B) shows a case where the lesions' presence, lateral extent and transmurality are clearly visible with the proposed imaging method, compared to uncertain identification and impossible delineation with a single wavelength.

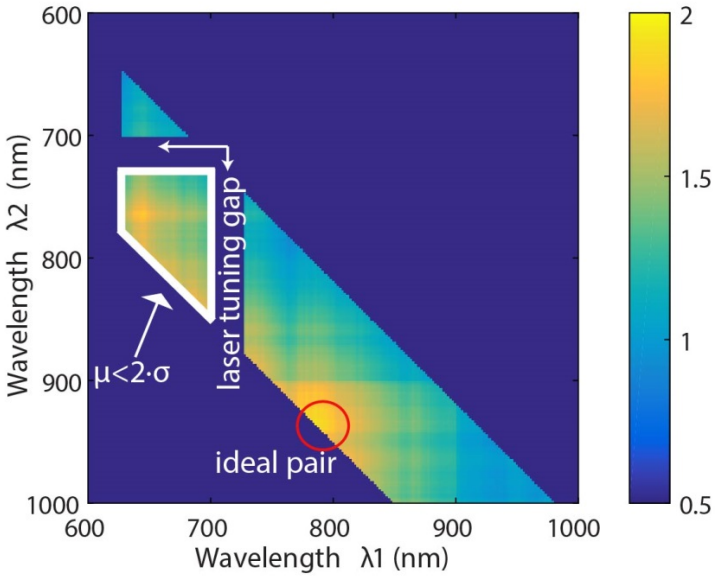

Fig. 6. $\varnothing_L / \varnothing_N$ over all eligible wavelengths.

Biomedical Optics EXPRESS

3.3.3 Quantitative performance evaluation

We quantitatively evaluate the performance of the proposed two-wavelength imaging technique by computing receiver-operator characteristic (ROC) curves. We apply different criteria for lesion identification and contrast, defined in 2.4.3. We compare two-wavelength imaging with two single-wavelength analyses, the optimal wavelength of 640 nm we identified based on the SR analysis, and 780 nm, which was previously identified as providing optimal contrast. The analysis is shown in Figs. 7(A) and 7(B).

The dual-wavelength analysis achieves an overall diagnostic accuracy of 0.97 for identification of lesions (comparing pre-/post-ablation) and also 0.97 for contrast (comparing lesions to neighboring control sites). The sensitivity and specificity at the operating point are 0.88 and 1.0, respectively, at a threshold of 0.39. The performance of any single wavelength imaging technique is inferior, with the optimal area under the curve (AUC) equal to 0.82 for lesion identification and 0.87 for contrast. We also find that 640 nm is consistently more effective than 780 nm for imaging RF ablation lesions.

The ROC analysis shows that the dual wavelength is more robust at detecting lesions. It also confirms that the dual wavelength imaging method proposed can highlight the lesion extent from the surrounding tissue better than a single wavelength imaging method.

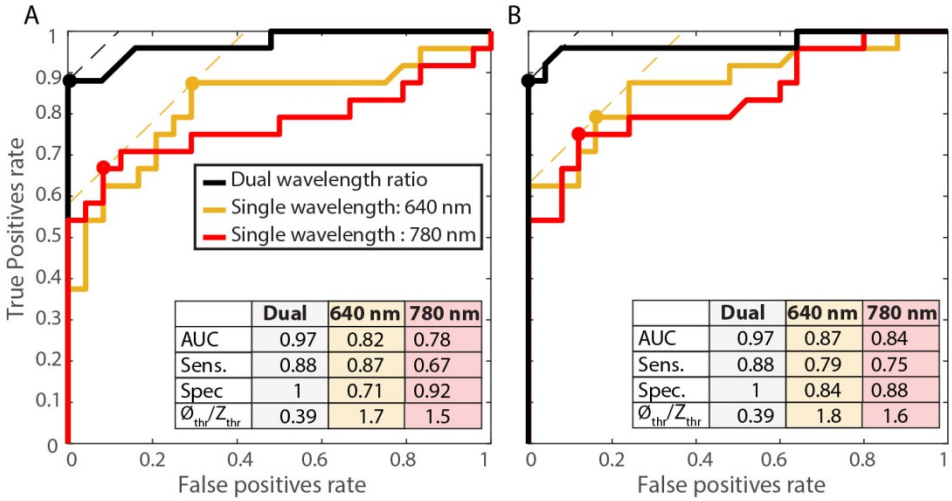

Fig. 7. Comparison between the Receiver Operating Characteristics (ROC) curves for lesion detection (A) and lesion contrast (B) of dual wavelength imaging, and single wavelength imaging at 640 and 780 nm. (AUC: area under the curve, Sens.: sensitivity, Spec.: specificity).

4. Discussion

4.1 Contribution of this work

In this work, we present a photoacoustic spectroscopic characterization of ablation lesions in left atrial tissue. We introduce a dual wavelength (790/930 nm) imaging method which forms an image based on two consecutive frames acquired at two optical wavelengths. Advantages over single wavelength imaging approaches presented before [19, 20] are insensitivity to fluence and temperature variations, resulting in more robust lesion detection, contrast and outlining (mainly transmurality). Quantitatively, we find that the best-performing single wavelength is 640 nm, in contrast to 780 nm that was suggested previously, based on qualitative assessment in single lesions [19].

We also found the reproducibility of lesion visibility with a single wavelength monitoring to be inferior to our proposed dual wavelength imaging method. Indeed, the proposed method reduces the number of false negatives making it a more suitable imaging method for both

Biomedical Optics EXPRESS

lesion formation monitoring and depth extent evaluation as well as for post-ablation mapping. The proposed method reduces the variability in signal strength due to the differences in tissue sites and geometry (trabeculae vs. smooth). Further studies will be needed to evaluate the balance between these benefits and the increased cost of dual wavelength imaging.

The signal change from 790 nm to 930 nm for lesions follows a negative slope, while that of untreated tissue is rather constant. The ratio of the signal at these two wavelengths is > 1 for lesions and ≈1 elsewhere. Blood has oxy/hemoglobin as its main chromophores, which are spectrally very similar to oxy/myoglobin. The absorption ratio at the chosen wavelengths is ≤ 1, making dual wavelength imaging more robust than single wavelength image in a blood environment, as it is based on highlighting signal from chromophores with a negative slope in that same range.

We confirm the spectral signature observed by Dana et al. [20], as well as the increase in signal from ablated tissue observed by Pang et al. [19]. However, we find that the correlation based imaging proposed in [20] highlights also the artefacts caused by image reconstruction and that the correlation to non-ablated tissue remains high making it difficult at instances to identify lesions from the rest of the tissue.

4.2 Interpretation of spectra

The main chromophores in healthy myocardium tissue are myoglobin, cytochrome c and hemoglobin in their reduced, oxygenated and oxidized states, as well as water, lipid and collagen. Myoglobin dominates the optical absorption response of cardiac tissue in the examined range but the contributions of lipid, water and collagen become more significant in the near infrared. Our spectroscopy results of non-ablated tissue do consistently reflect this mix of chromophores. We identified oxygenation effects in the shape of myoglobin features: The more the tissue is exposed to air, the more oxymyoglobin is formed. Therefore, the oxymyoglobin spectral signature in the visible range provides information on the freshness of the specimens received from the butcher. In fact, the flatness of the peak observed in our data set is representative of approximately 20% oxymyoglobin and 80% myoglobin on average. Sometimes there is also variability within the content of a sample (variation in tissue color Fig. 4(D)). Indeed, in Fig. 3, we note that the variability in SR_N is mainly representative of the variability of oxymyoglobin and myoglobin content of the tissue. The sharp variability observed at 690 and 660 nm could be associated with metmyoglobin formation.

RF ablation is a process where the tissue is heated over the transmission of radiofrequency current (~500kHz) through a resistive pathway to the indifferent electrode. The result of this process is the formation of coagulation necrosis associated with the denaturation of proteins [23]. Previous work on RF ablation lesion imaging based on optical methods, such as [24], reported lesions to be more optically scattering and to correspond better spectroscopically with the formation of metmyoglobin.. Metmyoglobin is an oxidized form of myoglobin (where the heme iron within the porphyrin ring is oxidized to Fe^{3+}) [25]. The rate of auto-oxidation of myoglobin is accelerated at higher temperatures under specific pH conditions. However, this state is reversible and is not an indication of proper lesion formation [26]. In the larger spectral range we investigated, we find that the optical absorption changes effected by ablation are not consistent with metmyoglobin formation. The denaturation process occurring during RF ablation is one in which proteins decompose and lose their spatial conformation. In the case of myoglobin, two of the resultants of such a process are denatured globin (optically transparent) and heme groups that form new compounds called hemichromes [27]. The spectrum we observe in lesions corresponds to that reported of hemichromes [28].

We performed our experiments on porcine cardiac tissue, which is a commonly used model for human cardiac tissue. We expect our proposed method to work on human tissue; indeed as reported by [10] the optical changes in porcine and human tissue due to ablation are similar with the human tissue being slightly more scattering. AF is often associated with an

Biomedical Optics EXPRESS

underlying disease called atrial fibrosis [29]. In this disease tissue is mechanically and structurally remodeled to contain more collagen; the targeted tissue is thus perhaps slightly different in structure and composition in comparison with the healthy pigs we have used. Nevertheless, the spectral absorption of collagen in the range of 790 to 930 nm would also yield a negative ratio value as opposed to the positive ratio value found for lesions. The denaturation of collagen results in gelatin [30] which would result in a positive ratio value [31], similar to the lesions we observed.

4.3 Future work and considerations for application

Future studies will explore the relation between ratio values and degree of ablation. Other studies such as [24, 32] noticed that the change in signal within the ranges of 600 to 700 nm, and 800 to 960 nm could possibly be an indicator of the degree of ablation. Moreover, we will also analyze lesion features on ultrasound for a more robust lesion assessment relying on a dual imaging modality scheme with the proposed PA dual wavelength imaging.

Finally, we have demonstrated the ability to visualize RF ablation lesions on ex vivo porcine tissue. We do anticipate similar results on cryo and microwave ablation lesions as they were reported to be histologically similar to RF ablation lesion [33]. Our setup likely has higher image resolution and greater sensitivity than can be expected from intracardiac echography probes, and represents a motionless and bloodless environment. Nevertheless, we foresee that our method should work in a clinical environment. Indeed, lesion formation is a slow process (~30, 60 s), and current laser repetition rates and pulse-to-pulse wavelength tuning should be enough to monitor ablation. Irrigated catheters effectively displace the blood at the ablation site. In order to translate this work to a more practical catheter based illumination setup, we will focus on dedicated catheters for PA-guided ablation.

5. Conclusion

We have characterized the photoacoustic signal from fresh and ablated porcine left atria tissue specimens over the range of 410 to 1000 nm. The changes we observe can be interpreted in terms of known irreversible processes occurring in thermal protein denaturation. We have demonstrated that imaging lesion formation using the ratio of two wavelengths achieves a diagnostic accuracy of 97% and displays a sensitivity of 88% and specificity of 100% at detecting and delineating lesions from the surrounding tissue, for an optimal wavelength pair of 790 and 930 nm. This method outperforms single-color imaging at any wavelength in the investigated range: ablated tissue generates a higher PA signal than untreated tissue but the variability in the enhancement is too large to provide reliable image contrast. Dual-wavelength ratio-based imaging removes the need of modeling the PA signal variation with tissue attenuation and temperature, which are relatively independent of temperature. The technique we explore in this study can be translated to intracardiac imaging with the application of modified ablation catheters for light delivery and ICE probes for signal detection.

Funding

Stichting voor de Technische Wetenschappen (STW) (12706).

Acknowledgements

The authors would like to thank Paul Knops, Robert Beurskens, Ayla Hoogendoorn, Maaike te Lintel Hekkert, Patricia Spicht, Klazina Kooiman and Richard van Duin for their help with the setup preparation.

Disclosure

The authors declare that there are no conflicts of interest related to this article.